analytical chemistry

pubs.acs.org/ac Article

Integration and Quantitative Visualization of 3,3′,5,5′-Tetramethylbenzidine-Probed Enzyme-Linked Immunosorbent Assay-like Signals in a Photothermal Bar-Chart Microfluidic Chip for Multiplexed Immunosensing

Guanglei Fu,* Ruixia Hou, Xianbo Mou, and Xiujun Li*

Cite This: *Anal. Chem.* 2021, 93, 15105−15114 Read Online

ACCESS | Metrics & More | Article Recommendations | Supporting Information

ABSTRACT: The photothermal effect shows significant promise for various biomedical applications but is rarely exploited for microfluidic lab-on-a-chip bioassays. Herein, a photothermal bar-chart microfluidic immunosensing chip, with the integration of the conventional 3,3′,5,5′-tetramethylbenzidine (TMB)-probed enzyme-linked immunosorbent assay (ELISA)-like system, was developed based on exploiting the photothermal pumping technique for visual bar-chart microfluidic immunosensing. Both the sandwich ELISA-like system and the photothermal pumping protocol were integrated into a single photothermal bar-chart chip. On-chip immunocaptured iron oxide nanoparticles catalyzed the oxidation of the chromogenic substrate, TMB, to produce a sensitive photothermal and chromogenic dual-functional probe, oxidized TMB. As the result of heat generation and the subsequent production of elevating vapor pressure in the sealed microfluidic environment, the on-chip near-infrared laser-driven photothermal effect of the probe served as a dose-dependent pumping force to drive the multiplexed quantitative display of the immunosensing signals as visual dye bar charts. Prostate-specific antigen as a model analyte was tested at a limit of detection of 1.9 ng·mL^{-1}, lower than the clinical diagnostic threshold of prostate cancer. This work presents a new perspective for microfluidic integration and multiplexed quantitative bar-chart visualization of the conventional TMB-probed ELISA signals possibly by means of an affordable handheld laser pointer in a lab-on-a-chip format.

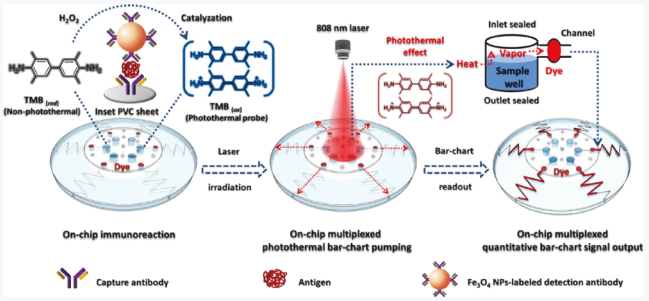

INTRODUCTION

Enzyme-linked immunosorbent assays (ELISAs) have long been established as one of the most conventional methodologies for various bioanalytical applications.[1,2] To transform the immunorecognition events into quantitative immunoassay signals, the involvement of specific signal transduction approaches, such as chromogenic reactions and fluorescence excitation, is usually essential in ELISAs.[3−5] In particular, 3,3′,5,5′-tetramethylbenzidine (TMB) has been one of the most popular chromogenic substrates in conventional ELISAs using horseradish peroxidase to catalyze the chromogenic reactions.[6] Various ready-to-run ELISA kits utilizing TMB-based chromogenic substrates are commercially available worldwide. A variety of artificial enzymes with peroxidase-mimic activities, such as iron oxide nanoparticles (NPs), have been explored for the development of TMB-probed ELISA-like immunoassays.[7−9] However, the signal output of these conventional ELISAs still relies on the employment of bulky and sophisticated spectrophotometers, compromising the potential for point-of-care (POC) detection. Therefore, there is an increasing trend of developing visual signal transduction methods.

The photothermal effect has recently emerged as a new signal transduction principle for visual biosensing.[10] Upon laser irradiation at required wavelengths, the photothermal agents can absorb the light energy and convert it into heat. The exploitation of photothermal agents as the specific biosensing probes offers an alternative way to quantitatively output the assay signals by means of portable temperature readers, such as thermometers.[11−13] A number of photothermal immunoassays have been developed based on implementing the photothermal tests in traditional vessels, such as microplates, polymerase chain reaction (PCR) tubes, and cuvettes.[10,14−16] Significantly, we for the first time discovered the near-infrared (NIR) laser-driven photothermal effect of the oxidation product of TMB and had developed a photothermal immunoassay using oxidized TMB as the photothermal probe in a conventional

Received: August 9, 2021
Accepted: October 25, 2021
Published: November 4, 2021

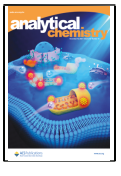

https://doi.org/10.1021/acs.analchem.1c03387
Anal. Chem. 2021, 93, 15105−15114

Scheme 1. Schematic Diagram of the Photothermal Bar-Chart Microfluidic Immunoassay[a]

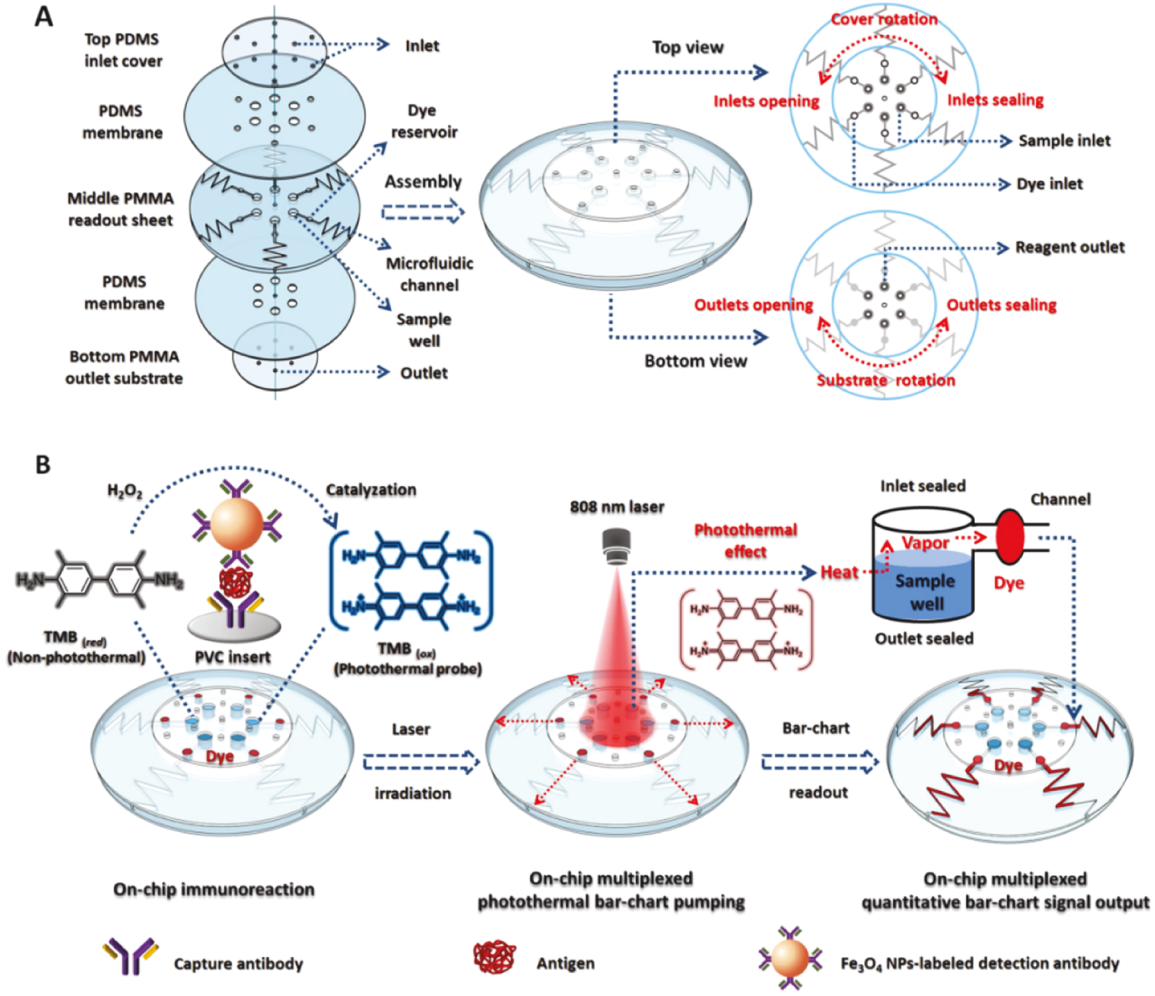

[a](A) Layout of the bar-chart chip; (B) multiplexed visual immunosensing on the photothermal bar-chart chip. The terminals of the sawtooth-shaped microfluidic channels are accessible to an air atmosphere at the lateral edge of the chip.

ELISA-like system.[6] Although simple quantitative readout of the assay signals using digital thermometers is enabled in these photothermal immunoassays, their applicability for POC detection is still challenged in aspects of insufficient integrability and deliverability of the photothermal testing settings, due to the complex tube-by-tube or well-by-well operations of laser irradiation and temperature measurement in these traditional vessels.[17] The integration of these photothermal immunoassays in miniaturized bioanalytical devices, such as microfluidic chips, presents a new perspective to realize visual photothermal immunosensing in a lab-on-a-chip format, which has rarely been reported to the best of our knowledge.

Microfluidics has become a powerful technology to provide miniaturized devices for lab-on-a-chip bioanalysis, attributed to the merits of integrability and portability of microfluidic devices.[18−21] Exploiting various working principles, microfluidic devices have shown considerable promise to prompt bioanalytical research.[22−25] Among these devices, the volumetric bar-chart chips are of increasing interest for POC bioassays because of the ease of straightforward on-chip output of quantitative distance-based assay signals in the form of visual ink bar charts.[26,27] The enzyme- or NP-catalyzed generation of gases is usually employed as the pumping force of the bar-chart movement of ink indicators in the chips.[26,27] Given the intrinsic features of the biological or chemical catalytic reactions, these bar-chart chips have to be confronted with several drawbacks, such as the complicated chip manufacturing and uncontrollability of the catalytic pumping performance once the chips are fixed up.[28] More importantly, to the best of our knowledge, most of these previously reported volumetric bar-chart chips are currently inapplicable to the popular TMB-probed assay systems. Based on applying the NP-mediated photothermal effect in bar-chart chips, we had reported a photothermal pumping technique for microfluidic transportation of liquid cargos.[28] The photothermal effect was explored as a robust and remotely controllable microfluidic pumping force to precisely drive the bar-chart movement of liquid cargoes with the aid of an affordable handheld laser pointer.[28] By loading the off-chip immunoassay solutions into the chips, we have recently developed a photothermal bar-chart chip to read the bar-chart quantification signals of the immunoassay solutions.[29] However, rather than a lab-on-a-chip format in this reported work, the sandwich ELISA-like procedure was performed in traditional PCR tubes with complicated off-chip NP conversion treatments, such as the ultrasonication of immunoreaction solutions.[29] Besides this, to visualize the bar-chart signals, the immunoassay solutions had to be mixed with the dye indicators before their on-chip

https://doi.org/10.1021/acs.analchem.1c03387
Anal. Chem. 2021, 93, 15105−15114

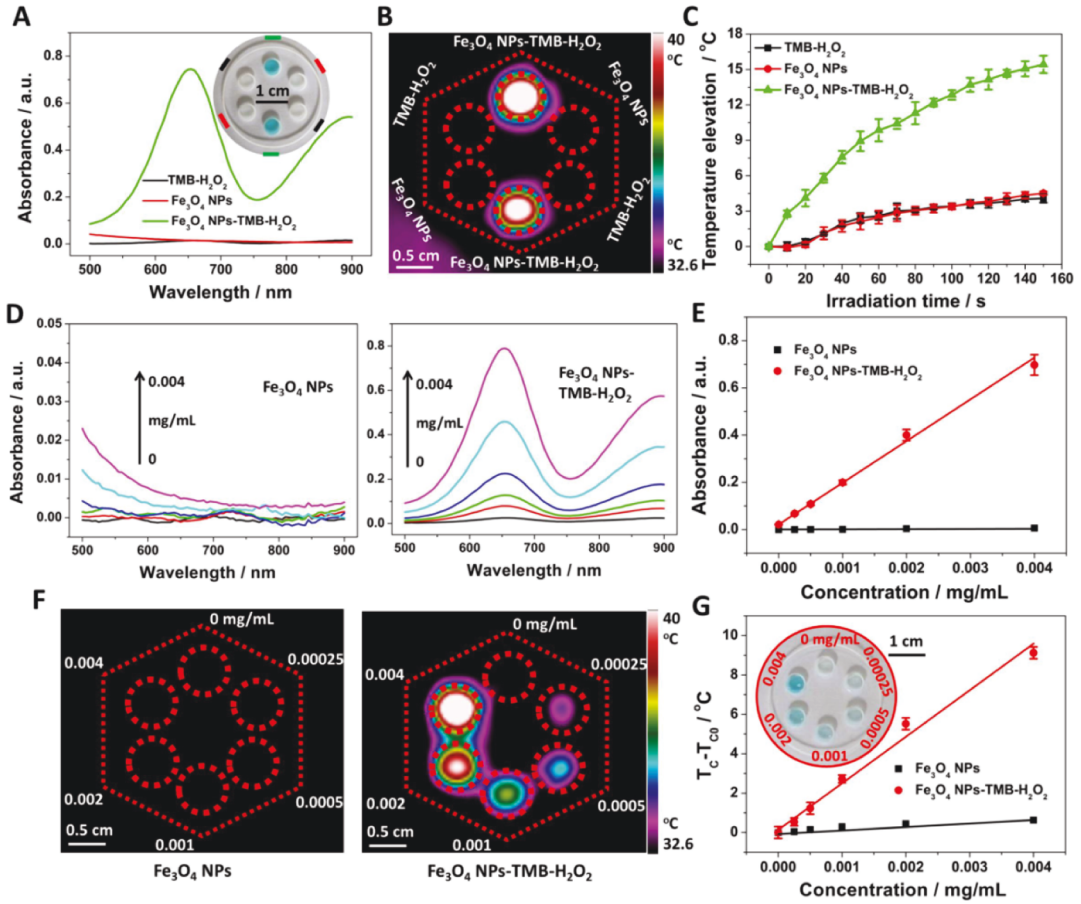

Figure 1. Off-chip photothermal investigations. (A) UV−vis absorption spectra of different chromogenic components (Fe_3O_4 NPs: 0.0040 mg·mL^{-1}); (B) thermal image of chromogenic components in a 6-well PMMA plate after laser irradiation for 60 s (1.1 W·cm^{-2}); (C) temperature variations of chromogenic components upon the irradiation for varying periods; (D) UV−vis absorption spectra of diverse concentrations of Fe_3O_4 NP dispersions with and without the chromogenic reactions; (E) absorbance at 650 nm as a function of the Fe_3O_4 NP concentration; (F) thermal images of reaction solutions after the irradiation for 60 s; and (G) temperature elevation value of reaction solutions as a function of the Fe_3O_4 NP concentration. Insets: photographs of reaction solutions in 6-well PMMA plates. Error bars represent standard deviations (n = 3).

loading into the same chambers,[29] making the method inapplicable to the TMB-probed assay systems due to the potential interference of the dye indicators to the susceptible chromogenic reactions.

Herein, with the on-chip integration of the conventional TMB-probed ELISA-like system, we develop a photothermal bar-chart microfluidic immunosensing chip based on exploiting the photothermal pumping technique for visual bar-chart microfluidic immunosensing. Employing a rotary switching design to control the microfluidic environment, both the sandwich ELISA-like system and the photothermal pumping protocol are integrated into a single poly(methyl methacrylate)/polydimethylsiloxane (PMMA/PDMS) bar-chart chip, as shown in Scheme 1. On-chip immunocaptured iron oxide NPs catalyze the oxidation of the chromogenic substrate, TMB, to produce a sensitive photothermal and chromogenic dual-functional probe, oxidized TMB. As the result of heat generation and the subsequent production of elevating vapor pressure in the sealed microfluidic environment, the on-chip NIR laser-driven photothermal effect of the probe serves as a dose-dependent pumping force to drive the multiplexed quantitative display of the immunosensing signals as visual dye bar charts. Using prostate-specific antigen (PSA) as a model analyte, the traditional spectrophotometric method was utilized to validate the immunosensing performance of the chips. In comparison with our published studies,[29] the new photothermal bar-chart immunosensing chip is more advantageous in the chip design and functionality (e.g., lab-on-a-chip integration of both the ELISA-like system and the photothermal pumping protocol), simplicity of operation (e.g., without complicated off-chip treatments of immunoreaction solutions), and particularly the applicability to the TMB-probed assay systems. Therefore, this work presents not only a new perspective for microfluidic integration and multiplexed quantitative bar-chart visualization of the conventional TMB-probed ELISA signals possibly by means of an affordable handheld laser pointer in a lab-on-a-chip format but also higher integrability and deliverability over the off-chip photothermal immunoassays.

EXPERIMENTAL SECTION

Materials and Instruments. PDMS was the product of Dow Corning (Midland, MI, USA). Laser irradiation was carried out using an 808 nm diode laser (LSR808H-10W-FC, Yueming Laser Technology Co., Ltd., Ningbo, China). Microfluidic patterns and chambers were carved in PMMA sheets using a laser engraver (MC-3020, Mingchuang Laser Equipment Co., Ltd., Liaocheng, China) (see details in the Supporting Information).

https://doi.org/10.1021/acs.analchem.1c03387
Anal. Chem. 2021, 93, 15105−15114

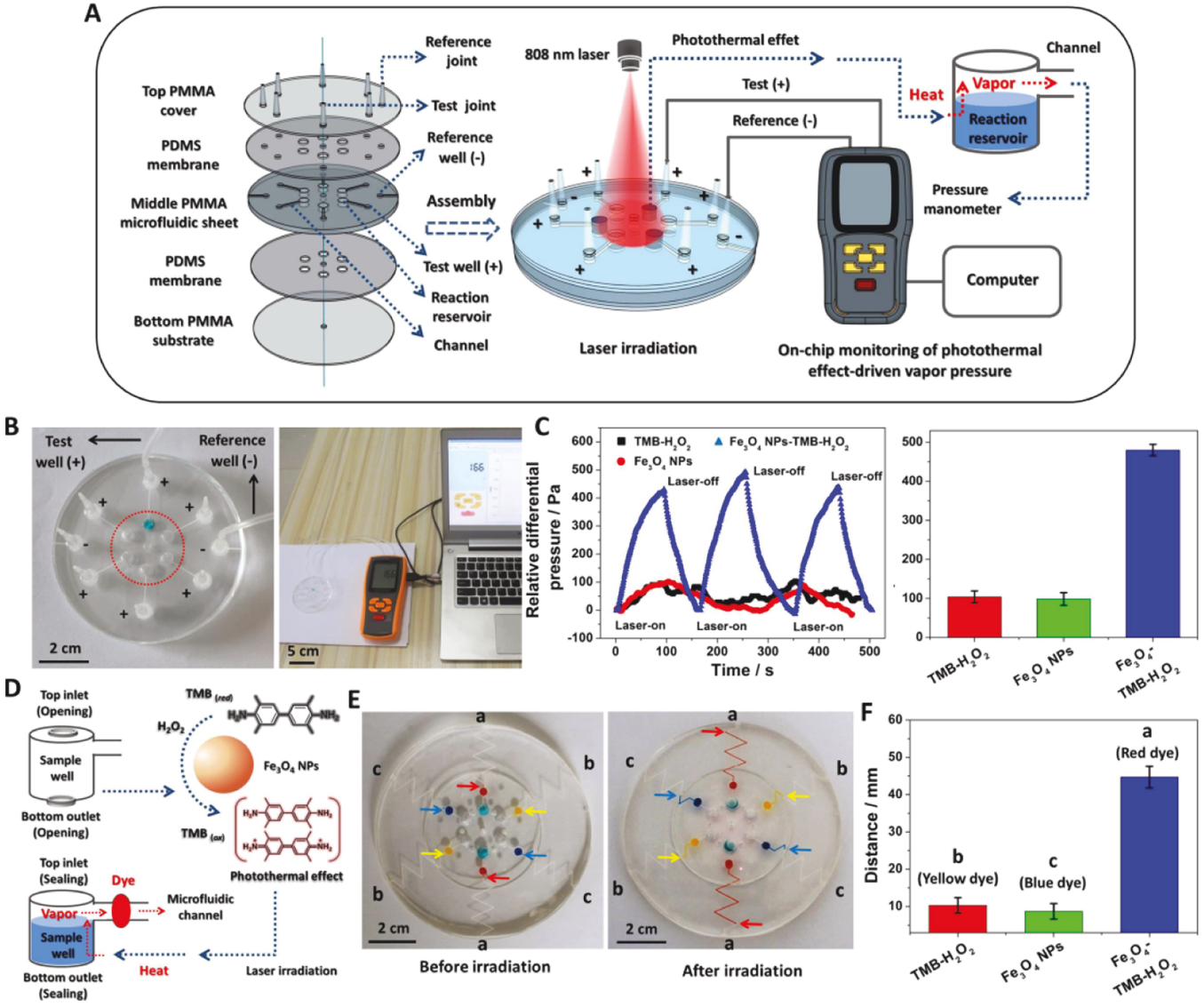

Figure 2. Principle of on-chip photothermal bar-chart pumping. (A) Schematic illustration of the pressure-monitoring platform; (B) photographic illustration of the pressure-monitoring chip and the platform; (C) on-chip pressure variations of different chromogenic components (Fe_3O_4 NPs: 0.0040 mg·mL^{-1}) upon a repeated laser-on (90 s, 1.5 W·cm^{-2}) and -off irradiation manipulation; (D) working principle of the photothermal bar-chart chip; (E) photographs of the bar-chart chip loaded with different chromogenic components before and after the irradiation for 90 s; and (F) bar-chart movement length. Different dye indicators mark diverse chromogenic components [i.e., a−c in (E,F)]. Arrows in all photographs of bar-chart chips in the article mark the terminal points of the dye bars. Error bars represent standard deviations (n = 3).

Layouts of Chips. Employing PDMS laminas as the adhesive sealing intersegments among PMMA sheets, all chip segments in each chip were concentrically stacked in sequence and simply stuck together with the alignment of relevant cavities to assemble the bar-chart chips. The top PDMS covers and bottom PMMA substrates of the chips can be detached and rotated to open or seal the inlets and outlets to handle reagents and to control the microfluidic environment (see details in the Supporting Information).

On-Chip Pressure Monitoring and Photothermal Investigations. An on-chip pressure-monitoring platform was used to monitor the resultant pressure variations in the chips during the laser irradiation of the chromogenic reaction solutions (see experimental details in the Supporting Information). In photothermal investigations using the bar-chart chips, the reaction solutions (60 μL per well) were loaded in the sample wells with sealed outlets. After loading the dye indicators in the dye reservoirs (8.0 μL per well), inlets of the bar-chart chips were sealed. The sample wells in the bar-chart chips were vertically irradiated for diverse periods at 1.5 W·cm^{-2}. In each irradiation manipulation, all sample wells in each chip were uniformly covered with a single laser spot of 2.8 cm diameter.

Photothermal Bar-Chart Microfluidic Immunoassay. After thorough cleaning, circular poly(vinyl chloride) (PVC) slices of 4.0 mm diameter were inserted into the sample wells of the bar-chart chips. Gentle washing of the sample wells with phosphate-buffered saline (0.01 M, pH 7.4) was conducted before applying new reagents in the immunoreaction procedures. To prevent the flow of these reagents into the microfluidic channels, all liquid reagents in the sample wells were loaded below the positions of the channels in the middle PMMA sheets of the bar-chart chips. A total of 50 μL of monoclonal anti-PSA antibody solutions (30 μg·mL^{-1}) were

https://doi.org/10.1021/acs.analchem.1c03387
Anal. Chem. 2021, 93, 15105−15114

pipetted into each sample well and incubated overnight at 4.0 °C. After blocking with 5.0% bovine serum albumin (BSA) solutions for 1.0 h, 50 μL of diverse concentrations of PSA solutions containing 1.0% human serum albumin was added and incubated for 1.0 h at room temperature. Subsequently, 50 μL of Fe_3O_4 NPs-labeled polyclonal anti-PSA antibody suspensions (0.25 mg·mL^{-1}) was added for further incubation for 1.0 h. Finally, 60 μL of TMB-H_2O_2 substrate solutions was pipetted into each sample well and reacted for 45 min, followed by removal of the PVC inserts, loading of dye indicators, and sealing of the bar-chart chips. The sample wells in each chip were irradiated for 120 s to monitor the bar-chart immunosensing signals (i.e., length of dye bar charts). UV−vis absorption spectra of the abovementioned immunoassay solutions were also recorded on a microplate reader.

RESULTS AND DISCUSSION

Off-Chip Photothermal Effect of the Chromogenic System. In this work, iron oxide (Fe_3O_4) NPs were used as the artificial peroxidase[6,7] to catalyze the chromogenic reaction between TMB and H_2O_2. The off-chip photothermal effect of the chromogenic system was studied by employing a 6-well PMMA plate (Figure S1) as the solution carrier under laser irradiation. Only in the existence of Fe_3O_4 NPs, the chromogenic substrate solutions (i.e., TMB-H_2O_2) exhibited quick color changes to blue (Figure 1A), indicating the occurrence of the typical Fe_3O_4 NP-catalyzed chromogenic reactions between TMB and H_2O_2. Meanwhile, an absorption peak appeared at 650 nm in UV−vis absorption spectra of the solutions, which was ascribed to the characteristic absorption band of the one-electron oxidation product of TMB (i.e., oxidized TMB in charge-transfer complexes).[6] It was worth noting that beyond the absorption band, oxidized TMB showed strong absorbance in the NIR light region from 750 to 900 nm with a potential photothermal effect.

To study the photothermal effect of oxidized TMB, the PMMA plates were vertically irradiated using an 808 nm diode laser. All wells in each plate were uniformly covered with a single laser beam in each irradiation manipulation. Thermal images of the plates were taken using a thermal camera after the irradiation. As shown in Figure 1B, the temperature signals of all solutions in the plate were recorded in a single thermal image. Only the Fe_3O_4 NP-catalyzed reaction solutions (i.e., Fe_3O_4 NPs-TMB-H_2O_2) displayed an obvious temperature elevation of up to 9.9 °C after the irradiation for 60 s, proving the strong photothermal effect of oxidized TMB in the reaction solutions.[6,16] As the irradiation period prolonged, the temperature of the reaction solutions elevated continuously (Figures 1C and S2). In contrast, the same concentrations of the other chromogenic components (i.e., Fe_3O_4 NPs and TMB-H_2O_2) exhibited minor temperature elevations of lower than 3.5 °C even after the irradiation for 100 s, attributed to their weak photothermal effects.

The photothermal effect of oxidized TMB was studied along with the optical absorption behavior as a function of the concentration of Fe_3O_4 NPs. With increasing concentrations of Fe_3O_4 NPs, the color of the Fe_3O_4 NP-catalyzed reaction solutions (i.e., Fe_3O_4 NPs-TMB-H_2O_2) gradually deepened in the PMMA plate (Figure 1G). The absorbance at 650 nm of the solutions increased linearly in the concentration range of 0.00025−0.0040 mg·mL^{-1} (Figure 1D,E), suggesting the generation of elevated concentrations of oxidized TMB in the reaction solutions. Fe_3O_4 NPs exhibited weak absorbance at each concentration alone. Consistent with the optical absorption behavior, upon the laser irradiation for 60 s, the temperature signals of the Fe_3O_4 NP-catalyzed reaction solutions elevated linearly with the Fe_3O_4 NP concentration (Figure 1F,G). These results demonstrated that oxidized TMB was not only a conventional chromogenic probe but also a photothermal probe.

Principle of On-Chip Photothermal Bar-Chart Pumping. The photothermal effect of oxidized TMB was expected to serve as the pumping force of bar-chart microfluidic signals. To reveal the on-chip photothermal pumping principle, a pressure-monitoring platform was designed as shown in Figure 2A. In the hybrid chip, PDMS laminas worked as the adhesive sealing intersegments among PMMA sheets including (1) a bottom PMMA sealing substrate; (2) a middle PMMA sheet carved with central reservoirs, peripheral reference and test wells, and channels; and (3) a top PMMA sealing cover stuck with joints to the wells. The chromogenic reaction took place in the central reservoirs that were individually accessible to relevant test wells through channels, while the reference wells were solely accessible to an air atmosphere. Joints of the reference and test wells were interfaced to a differential pressure manometer. In such a sealed pathway, the real-time pressure variations in the central reservoirs can be monitored on a manometer with synchro data output in a computer terminal (Figure 2B).

The central reservoirs were vertically irradiated using the laser for 90 s. Only the Fe_3O_4 NP-catalyzed reaction solutions exhibited a substantial elevation of up to 480 Pa in the differential pressure value (Figure 2C). In contrast, unapparent elevations of lower than 104 Pa were monitored from the other chromogenic components with weak photothermal effects. Furthermore, upon a repeated laser-on and -off manipulation, the on-chip pressure strength can be harvested in accordance with the manipulation. Due to the photothermal effect of oxidized TMB in central reservoirs under the laser irradiation, rapid heat generation in the reaction solutions resulted in the production of elevating vapor pressure in the sealed microfluidic environment.[28]

To investigate the possibility of the photothermal effect as the pumping force of bar-chart signals, we further modified the pressure-monitoring chip to a bar-chart chip (Scheme 1A). Sawtooth-shaped channels individually accessible to the sample wells and dye reservoirs were carved in the middle PMMA sheets. Inlets and outlets were punched on the top PDMS covers and the bottom PMMA substrates, respectively. By detaching and rotating the top and bottom segments to open or seal relevant cavities, inlets and outlets can be switched on or off to handle reagents and to control the microfluidic environment. In the sealed microfluidic pathway with the loading of reaction solutions (i.e., in sample wells) and the corresponding dye indicators (i.e., in dye reservoirs), vapor pressure produced by the photothermal effect of oxidized TMB in the sample wells can drive the movement of dye indicators in the sawtooth-shaped channels (Figure 2D). As expected, upon the irradiation of all sample wells in each chip with a single laser beam, movements of dye indicators in the channels were vividly displayed as visual dye bar charts in a multiplexed way (Figure 2E). In good agreement with the aforementioned photothermal and pressure investigations, the Fe_3O_4 NP-catalyzed reaction solutions resulted in fast bar-chart movements of dye indicators of around 44 mm length (Figure 2F), whereas the other chromogenic components showed negligible

https://doi.org/10.1021/acs.analchem.1c03387
Anal. Chem. 2021, 93, 15105−15114

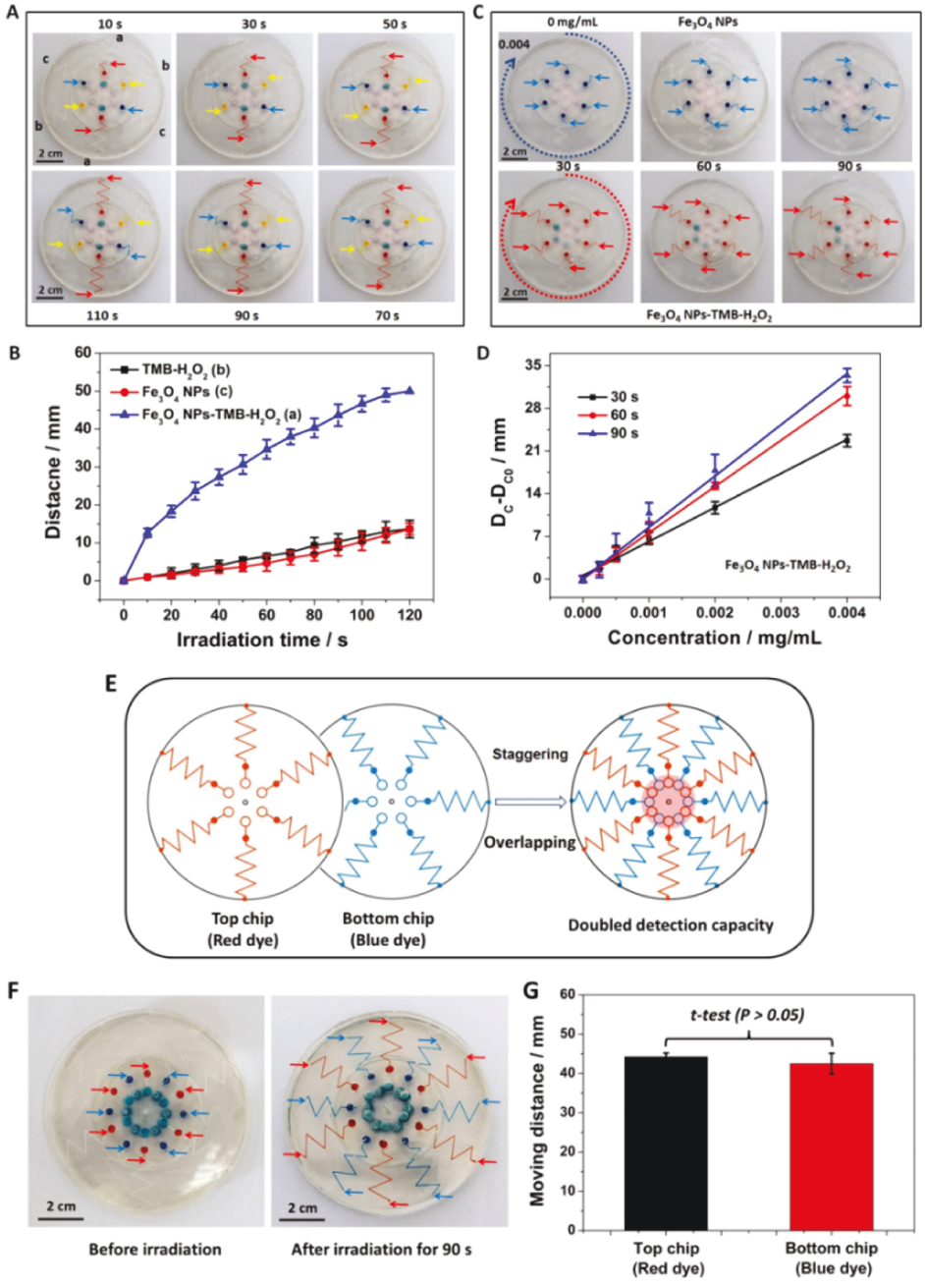

Figure 3. Performance of output of photothermal bar-chart signals. (A) Photos of bar-chart chips loaded with different chromogenic components (Fe_3O_4 NPs: 0.0040 mg·mL^{-1}) upon the laser irradiation for diverse periods (1.5 W·cm^{-2}); (B) bar-chart movement length; (C) photos of bar-chart chips with varying concentrations of Fe_3O_4 NP dispersions with (red indicator) and without (blue indicator) the chromogenic reactions upon irradiation for diverse periods; (D) bar-chart movement length as a function of the Fe_3O_4 NP concentration; (E) strategy to achieve doubled detection capacity; (F) photos of two concentrically staggered bar-chart chips before and after irradiation for 90 s (bottom chip: blue indicator, top chip: red indicator); and (G) bar-chart movement length. Different dye indicators mark diverse chromogenic components [i.e., a−c in (A,B)]. Error bars represent standard deviations (n = 3).

bar-chart movements. Therefore, the on-chip photothermal effect of oxidized TMB can act as the pumping force of visual bar-chart signals in the chips.

Performance of On-Chip Output of Photothermal Bar-Chart Signals. The uniformity of microfluidic channels for liquid flow (i.e., dye indicators) in the photothermal bar-chart chips was first characterized (Figure S3). The effects of irradiation time and concentration of Fe_3O_4 NPs on the photothermal bar-chart signals (i.e., bar-chart traveling length of dye indicators) were then studied in the bar-chart chips. The chips loaded with diverse chromogenic components and dye indicators were irradiated for varying periods. With the prolonging of the irradiation period, the bar-chart signals of the Fe_3O_4 NP-catalyzed reaction solutions rose continuously in the two symmetrical channels (Figure 3A,B). Similarly, the same concentrations of the other chromogenic components showed much lower bar-chart signals at all irradiation times. The results suggested that the photothermal bar-chart signal can be remotely controlled by manipulating the irradiation period.

https://doi.org/10.1021/acs.analchem.1c03387
Anal. Chem. 2021, 93, 15105−15114

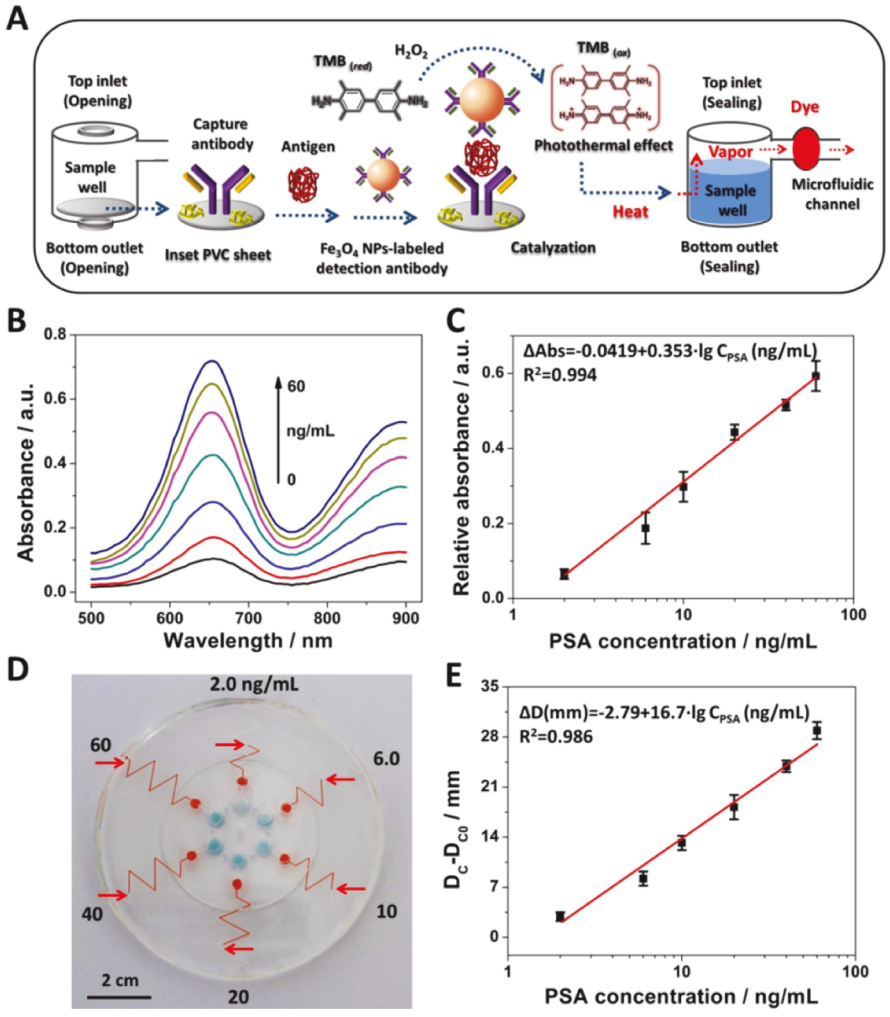

Figure 4. Photothermal bar-chart microfluidic immunoassay. (A) Schematic diagram of the photothermal bar-chart microfluidic immunoassay; (B) UV−vis absorption spectra of immunoassay solutions acquired from varying concentrations of PSA; (C) calibration plot (ΔAbs vs lg C_{PSA}) of the spectrophotometric method for PSA determination; (D) photograph of the bar-chart immunoassay chip upon the laser irradiation for 120 s (1.5 W·cm^{-2}); and (E) calibration plot (ΔD vs lg C_{PSA}) of the bar-chart chip for PSA determination. Error bars represent standard deviations (n = 3).

The reaction solutions catalyzed by varying concentrations of Fe_3O_4 NPs were irradiated for different periods in the same bar-chart chip. Increasing bar-chart signals of the reaction solutions were monitored as the concentration of Fe_3O_4 NPs elevated at each irradiation time (Figure 3C,D), owing to the dose-dependent photothermal pumping behavior. In contrast, Fe_3O_4 NPs exhibited weak bar-chart signals alone because of the weak photothermal effect (Figure S4). The bar-chart signals of the reaction solutions were linearly associated with the Fe_3O_4 NP concentration in the range of 0.00025−0.0040 mg·mL^{-1} at three irradiation times, which provided a quantification basis for bioanalytical applications of the photothermal bar-chart chip.

Taking advantage of the transparent chip matrices under laser irradiation, the detection capacity of the photothermal bar-chart chip can be flexibly doubled by the simple concentric staggering of two overlapped chips (Figure 3E). In this way, 12 sample wells on the two planes can be alternatively positioned in the same transparent spatial region. Using different dye indicators to distinguish the upper and lower bar-chart signals, all sample wells loaded with the same concentration of the reaction solutions in the two chips were exposed to a single laser spot. Interestingly, both chips exhibited uniform bar-chart signals (Figure 3F), and no significant difference was observed between the bar-chart signals in the two chips (Figure 3G). These results demonstrated the feasibility of the strategy in doubling the detection capacity in each test.

Photothermal Bar-Chart Microfluidic Immunoassay. The conventional TMB-probed ELISA-like system was integrated into the photothermal bar-chart chip for visual microfluidic immunosensing using PSA as a model analyte. The sandwich immunoreaction procedure was performed on the surface of PVC inserts in the sample wells, where Fe_3O_4 NP-labeled antibodies worked as the detection element. With the aid of the rotary switching design to handle reagents and to control the microfluidic environment, both the TMB-probed ELISA-like system and the photothermal pumping protocol were integrated into a single photothermal bar-chart chip, as illustrated in Figure 4A.

To validate the analytical performance of the photothermal bar-chart immunosensing chip, the traditional off-chip spectrophotometric method was also employed to read the immunoassay signals. After the on-chip immunoreaction and chromogenic reaction, the absorbance of the immunoassay solutions at 650 nm was recorded on a microplate reader. As the PSA concentration elevated, the relative absorbance (i.e.,

https://doi.org/10.1021/acs.analchem.1c03387
Anal. Chem. 2021, 93, 15105−15114

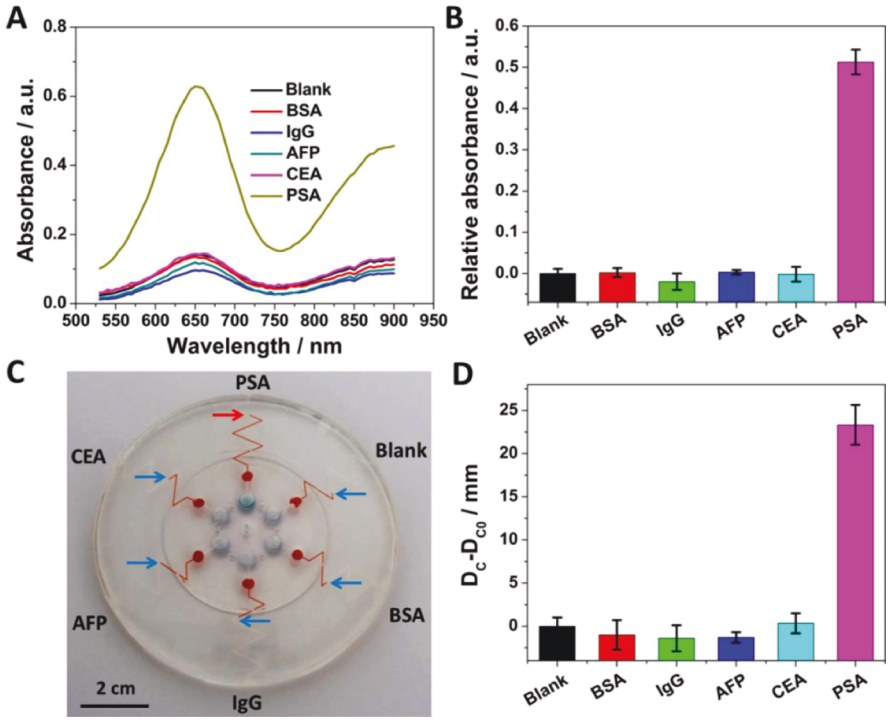

Figure 5. Selectivity of the photothermal bar-chart immunosensing chip. (A) UV−vis absorption spectra of immunoassay solutions acquired from diverse biomolecules (PSA: 40 ng·mL^{-1}, BSA: 100 μg·mL^{-1}, IgG: 100 μg·mL^{-1}, AFP: 200 ng·mL^{-1}, CEA: 200 ng·mL^{-1}); (B) relative absorbance (ΔAbs) at 650 nm; (C) photograph of the bar-chart immunoassay chip upon the laser irradiation for 120 s (1.5 W·cm^{-2}); and (D) relative bar-chart movement distance (ΔD). Error bars represent standard deviations (n = 3).

$Abs_C - Abs_{C_0} = \Delta Abs$) increased linearly with the logarithm of PSA concentration in the range of 2.0−60 ng·mL^{-1} (R^2 = 0.994) (Figure 4B,C), indicating the on-chip binding of elevating amounts of detection antibody in the ELISA-like system. The sample wells in the chips were irradiated to implement the on-chip photothermal bar-chart pumping. Significantly, multiplexed immunosensing signals were quantitatively displayed as visual dye bar charts in the chips (Figures 4D,E and S5). The relative bar-chart signals (i.e., $D_C - D_{C_0} = \Delta D$) were proportional to the logarithm of PSA concentration in the same range (R^2 = 0.986). The photothermal bar-chart readout results were consistent with those of the traditional spectrophotometric method, which was attributed to the direct correlation of both methods with the level of the same probe, oxidized TMB, in the immunoassay system.

The spectrophotometric and photothermal bar-chart readout methods showed comparable limits of detection (LODs) of 1.4 and 1.9 ng·mL^{-1} (S/N = 3) in PSA determination, respectively. Although the LOD of the bar-chart chip was slightly higher than that of some previously reported spectrophotometric ELISAs (i.e., 1.0 ng·mL^{-1})[30] and off-chip photothermal immunoassays (i.e., 1.0 ng·mL^{-1}),[6,10] it still fell below the clinical diagnostic threshold (i.e., 4.0 ng·mL^{-1})[30] of prostate cancer in PSA determination. These results implied the potential applicability of the chip for clinical diagnostics. In contrast to these previous studies,[14,31−35] the photothermal bar-chart chip presents not only quantitative bar-chart visualization of the ELISA signals in a lab-on-a-chip format without utilizing bulky and sophisticated spectrophotometers but also higher integrability and deliverability over the off-chip photothermal immunoassays.

Selectivity and Analysis of Real Serum Samples. To verify the selectivity of the photothermal bar-chart chip for PSA determination, some interfering biomolecules, such as human immunoglobulin G (IgG), α-fetoprotein (AFP), and carcinoembryonic antigen (CEA), were tested in parallel with PSA. As shown in Figure 5, only PSA showed distinct immunosensing signals (i.e., $Abs_C - Abs_{C_0}$ and $D_C - D_{C_0}$) in both methods. The results verified the remarkable selectivity of the photothermal bar-chart chip in PSA determination, owing to the high specificity of the on-chip immunorecognition process. Additionally, the bar-chart chip showed good precision and reproducibility in intra- and inter-immunoassays (Figures S6 and S7).

The standard addition method was utilized to assess the accuracy of the photothermal bar-chart chip in the analysis of real serum samples. Normal human serums were spiked with varying concentrations of PSA solutions and were then tested in the chip using the traditional spectrophotometric method for validation of the analytical results. Both methods presented comparable analytical recoveries of PSA quantification results in the range of 93−105% (Tables S1 and S2), which fell within the generally adopted criteria (i.e., 90−110%, RSD ≤ 15%) in the validation of bioassays,[36] demonstrating acceptable accuracy of the photothermal bar-chart chip in real-sample analysis.

CONCLUSIONS

A new photothermal bar-chart microfluidic immunosensing chip is developed based on exploiting the photothermal pumping technique for visual microfluidic immunosensing. Both the conventional TMB-probed ELISA-like system and the photothermal pumping protocol are integrated into a single photothermal bar-chart chip to enable the straightforward

https://doi.org/10.1021/acs.analchem.1c03387
Anal. Chem. 2021, 93, 15105−15114

output of quantitative bar-chart immunosensing signals. Using the traditional spectrophotometric method for validation, the photothermal bar-chart chip shows acceptable immunosensing performance in PSA determination. This work presents a new perspective for microfluidic integration and multiplexed quantitative bar-chart visualization of the conventional TMB-probed ELISA signals possibly by means of an affordable handheld laser pointer in a lab-on-a-chip format. Additionally, this work provides higher integrability and deliverability of the photothermal testing settings over the off-chip photothermal immunoassays. The multiplexed detection of more samples in a single chip can be achieved by on-demand modifying the chip layout and magnifying the size of the laser spot. To the best of our knowledge, most previously reported volumetric bar-chart chips are currently inapplicable to the TMB-probed assay systems. In comparison with the volumetric bar-chart chips, the photothermal bar-chart chips offer (1) simpler and lower cost chip manufacturing (e.g., without complicated microfluidic patterning on glass matrixes using cleanroom facilities); (2) easier controllability toward the bar-chart pumping performance by remotely manipulating the irradiation parameters; and (3) higher compatibility with a variety of commercial ELISA kits using TMB-based chromogenic substrates (e.g., no need to prepare additional specific materials, such as catalase- or platinum NP-conjugated antibodies). Given that TMB is one of the most popular chromogenic substrates in various bioanalytical settings,[13,37−39] a wide range of these conventional bioassays can be flexibly introduced in the platform to implement diverse lab-on-a-chip biosensing tasks.

■ ASSOCIATED CONTENT

Supporting Information

The Supporting Information is available free of charge at https://pubs.acs.org/doi/10.1021/acs.analchem.1c03387.

Details of chip layouts, off-chip chromogenic reaction, on-chip pressure monitoring, characterization of uniformity of microfluidic channels, precision and reproducibility, and results of real-sample analysis (PDF)

■ AUTHOR INFORMATION

Corresponding Authors

Guanglei Fu − *Biomedical Engineering Research Center, Medical School of Ningbo University, Ningbo 315211 Zhejiang, P. R. China;* orcid.org/0000-0002-8128-1224; Email: fuguanglei@nbu.edu.cn

Xiujun Li − *Department of Chemistry and Biochemistry, The University of Texas at El Paso, El Paso, Texas 79968, United States;* orcid.org/0000-0002-7954-0717; Email: xli4@utep.edu

Authors

Ruixia Hou − *Biomedical Engineering Research Center, Medical School of Ningbo University, Ningbo 315211 Zhejiang, P. R. China*

Xianbo Mou − *Biomedical Engineering Research Center, Medical School of Ningbo University, Ningbo 315211 Zhejiang, P. R. China*

Complete contact information is available at: https://pubs.acs.org/10.1021/acs.analchem.1c03387

Notes

The authors declare no competing financial interest.

■ ACKNOWLEDGMENTS

We are grateful for the financial supports from the National Natural Science Foundation of China (nos. 81701790 and no. 32000942), the Natural Science Foundation of Zhejiang Province (no. LY20C100001), the U.S. NIH/NIAID (no. R21AI107415), the U.S. NSF (no. IIP2052347 and no. IIP2122712), the CPRIT (no. RP210165), and the U.S. DOT (CARTEEH).

■ REFERENCES

(1) Verma, M. S.; Tsaloglou, M.-N.; Sisley, T.; Christodouleas, D.; Chen, A.; Milette, J.; Whitesides, G. M. *Biosens. Bioelectron.* **2018**, *99*, 77−84.
(2) Wang, Z.; Zong, S.; Wu, L.; Zhu, D.; Cui, Y. *Chem. Rev.* **2017**, *117*, 7910−7963.
(3) Sanjay, S. T.; Dou, M.; Sun, J.; Li, X. J. *Sci. Rep.* **2016**, *6*, 30474.
(4) Wang, S.; Ge, L.; Song, X.; Yu, J.; Ge, S.; Huang, J.; Zeng, F. *Biosens. Bioelectron.* **2012**, *31*, 212−218.
(5) Kim, S.; Chun, H. J.; Lee, K. W.; Yoon, H. C. *Biosens. Bioelectron.* **2020**, *150*, 111932.
(6) Fu, G.; Sanjay, S. T.; Zhou, W.; Brekken, R. A.; Kirken, R. A.; Li, X. *Anal. Chem.* **2018**, *90*, 5930−5937.
(7) Woo, M.-A.; Kim, M.; Jung, J.; Park, K.; Seo, T.; Park, H. *Int. J. Mol. Sci.* **2013**, *14*, 9999−10014.
(8) Ye, H.; Yang, K.; Tao, J.; Liu, Y.; Zhang, Q.; Habibi, S.; Nie, Z.; Xia, X. *ACS Nano* **2017**, *11*, 2052−2059.
(9) Wang, C.; Gao, J.; Tan, H. *ACS Appl. Mater. Interfaces* **2018**, *10*, 25113−25120.
(10) Fu, G.; Sanjay, S. T.; Dou, M.; Li, X. *Nanoscale* **2016**, *8*, 5422−5427.
(11) Zhou, W.; Hu, K.; Kwee, S.; Tang, L.; Wang, Z.; Xia, J.; Li, X. *Anal. Chem.* **2020**, *92*, 2739−2747.
(12) Zhou, W.; Sun, J.; Li, X. *Anal. Chem.* **2020**, *92*, 14830−14837.
(13) Yi, D.; Wei, Z.; Zheng, W.; Pan, Y.; Long, Y.; Zheng, H. *Sens. Actuators, B* **2020**, *323*, 128691.
(14) Wei, Y.; Wang, D.; Zhang, Y.; Sui, J.; Xu, Z. *Biosens. Bioelectron.* **2019**, *140*, 111345.
(15) Cai, G.; Yu, Z.; Tong, P.; Tang, D. *Nanoscale* **2019**, *11*, 15659−15667.
(16) Huang, L.; Chen, J.; Yu, Z.; Tang, D. *Anal. Chem.* **2020**, *92*, 2809−2814.
(17) Fu, G.; Li, X.; Wang, W.; Hou, R. *Biosens. Bioelectron.* **2020**, *170*, 112646.
(18) Zhou, W.; Dou, M.; Timilsina, S. S.; Xu, F.; Li, X. *Lab Chip* **2021**, *21*, 2658−2683.
(19) Sanjay, S. T.; Fu, G.; Dou, M.; Xu, F.; Liu, R.; Qi, H.; Li, X. *Analyst* **2015**, *140*, 7062−7081.
(20) Mou, L.; Jiang, X. *Adv. Healthcare Mater.* **2017**, *6*, 1601403.
(21) Tavakoli, H.; Zhou, W.; Ma, L.; Perez, S.; Ibarra, A.; Xu, F.; Zhan, S.; Li, X. *Trends Anal. Chem.* **2019**, *117*, 13−26.
(22) Zhou, W.; Feng, M.; Valadez, A.; Li, X. J. *Anal. Chem.* **2020**, *92*, 7045−7053.
(23) Li, X.; Liu, X. *Adv. Healthcare Mater.* **2016**, *5*, 1326−1335.
(24) Hu, B.; Li, J.; Mou, L.; Liu, Y.; Deng, J.; Qian, W.; Sun, J.; Cha, R.; Jiang, X. *Lab-on-a-Chip* **2017**, *17*, 2225−2234.
(25) Zhang, H.; Yu, X.; Liu, Y.; Lin, B.; Jiang, M.; Song, J.; Di, W.; Zhu, Z.; Yang, C. *Anal. Chem.* **2021**, *93*, 7235−7241.
(26) Zhu, Z.; Guan, Z.; Jia, S.; Lei, Z.; Lin, S.; Zhang, H.; Ma, Y.; Tian, Z.-Q.; Yang, C. J. *Angew. Chem., Int. Edit.* **2014**, *53*, 12503−12507.
(27) Wei, X.; Zhou, W.; Sanjay, S. T.; Zhang, J.; Jin, Q.; Xu, F.; Dominguez, D. C.; Li, X. *Anal. Chem.* **2018**, *90*, 9888−9896.
(28) Fu, G.; Zhou, W.; Li, X. *Lab-on-a-Chip* **2020**, *20*, 2218−2227.
(29) Zhou, W.; Fu, G.; Li, X. *Anal. Chem.* **2021**, *93*, 7754−7762.
(30) Gao, Z.; Hou, L.; Xu, M.; Tang, D. *Sci. Rep.* **2014**, *4*, 3966.

(31) Du, S.; Wang, Y.; Liu, Z.; Xu, Z.; Zhang, H. *Biosens. Bioelectron.* **2019**, *144*, 111670.
(32) Huang, L.; Yu, Z.; Chen, J.; Tang, D. *ACS Appl. Bio Mater.* **2020**, *3*, 9156−9163.
(33) Ren, R.; Cai, G.; Yu, Z.; Zeng, Y.; Tang, D. *Anal. Chem.* **2018**, *90*, 11099−11105.
(34) Hong, G.; Zhang, D.; He, Y.; Yang, Y.; Chen, P.; Yang, H.; Zhou, Z.; Liu, Y.; Wang, Y. *Anal. Bioanal. Chem.* **2019**, *411*, 6837−6845.
(35) Luo, Z.; Qi, Q.; Zhang, L.; Zeng, R.; Su, L.; Tang, D. *Anal. Chem.* **2019**, *91*, 4149−4156.
(36) Zhou, S.; Zheng, W.; Chen, Z.; Tu, D.; Liu, Y.; Ma, E.; Li, R.; Zhu, H.; Huang, M.; Chen, X. *Angew. Chem., Int. Edit.* **2014**, *53*, 12498−12502.
(37) An, P.; Rao, H.; Gao, M.; Xue, X.; Liu, X.; Lu, X.; Xue, Z. *Chem. Commun.* **2020**, *56*, 9799−9802.
(38) Gao, Z.; Xu, M.; Hou, L.; Chen, G.; Tang, D. *Anal. Chem.* **2013**, *85*, 6945−6952.
(39) Gao, Z.; Tang, D.; Tang, D.; Niessner, R.; Knopp, D. *Anal. Chem.* **2015**, *87*, 10153−10160.

https://doi.org/10.1021/acs.analchem.1c03387
Anal. Chem. 2021, 93, 15105−15114